Machine Learning-Guided Optimization of Coercive Field in $Al_{1-x}Sc_xN$ Thin Films for Non-Volatile Memory

Shaon Das[1], Prachi Garg[1], and Baishakhi Mazumder[1, *]

[1] *Department of Materials Design and Innovation, University at Buffalo-SUNY, Buffalo, NY 14260, USA*

* *Corresponding author: baishakh@buffalo.edu*

Abstract:

This study employs a data-driven machine learning approach to investigate specific ferroelectric properties of $Al_{1-x}Sc_xN$ thin films, targeting their application in next-generation non-volatile memory (NVM) devices. This approach analyzes a vast design space, encompassing over a million data points, to predict a wide range of coercive field values that are crucial for optimizing $Al_{1-x}Sc_xN$-based NVM devices. We evaluated seven machine learning models to predict the coercive field across a range of conditions, identifying the random forest algorithm as the most accurate, with a test R^2 value of 0.88. The model utilized five key features: film thickness, measurement frequency, operating temperature, scandium concentration, and growth temperature to predict the design space. Our analysis spans 13 distinct scandium concentrations and 13 growth temperatures, encompassing thicknesses from 9nm to 1000nm, frequencies from 1kHz to 100kHz, and operating temperatures from 273K to 700K. The predictions revealed dominant coercive field values between 3.0 MV/cm to 4.5 MV/cm, offering valuable insights for the precise engineering of $Al_{1-x}Sc_xN$-based NVM devices. This work underscores the potential of machine learning in guiding the development of advanced ferroelectric materials with tailored properties for enhanced device performance.

Keywords: ferroelectricity; coercive field; supervised ml; aluminum scandium nitride; thin film.

I. Introduction

Ferroelectric materials, characterized by their non-centrosymmetric crystal structure, exhibit spontaneous polarization resulting from the alignment of dipole moments along a particular spatial direction. This unique property grants these materials distinctive electrical characteristics, such as resistive switching and energy storage.[1-3] The spontaneous polarization is known to be altered under the influence of an external electric field which makes them attractive candidates for non-volatile memory devices like FE field-effect transistors (FeFET), FE tunnel junction (FTJ), FE random access memory (FeRAM), etc.[4-7] High switching speed and endurance in oxide perovskites made them one of the most widely used ferroelectric materials in the market since the 1990s have faced numerous drawbacks, which led to the development of fluorite-structured ferroelectrics in 2006.[1, 2, 4, 8-15] However, continuous research is necessary to discover new ferroelectric materials that can withstand harsh environmental conditions and enhance the scalability.

III-nitride semiconductors (AlN, GaN) doped with rare earth metals like Sc and B exhibit strong ferroelectric polarization switching, offering enhanced performance, scalability, and suitability for harsh environment applications compared to other ferroelectric materials.[1, 16, 17] This finding was unexpected, as the coercive field (E_c) and dielectric breakdown field (E_{bd}) are very close for III-nitride-based semiconductors, coupled with the paucity of experiments conducted under a large external electric field.[2, 4, 18] Wurtzite-structured aluminum scandium nitride ($Al_{1-x}Sc_xN$) is one of the prominent nitride-ferroelectric materials studied widely since its discovery in 2019.[1, 4] The introduction of scandium (Sc) in aluminum nitride (AlN) can flatten the Gibbs free-energy landscape of the III-nitride wurtzite structure, leading to the transformation of conventional III-nitrides into ferroelectrics.[1, 19-22] Over the last decade, $Al_{1-x}Sc_xN$ has been the subject of extensive study following the 2009 discovery of its high piezoelectric coefficient by Akiyama et al. and for its piezoelectric-based applications.[23-31] However, its significance goes beyond piezoelectricity after the discovery of its ferroelectric properties. In the realm of ferroelectric materials, two crucial properties—remnant polarization (Pr) and coercive field (Ec)—are widely examined for evaluating the performance of ferroelectric materials in non-volatile memory applications. Here, Pr defines the on/off ratio, representing the reliability and efficiency of data storage in binary form, while Ec determines the size of the memory window.[32] In most of the memory-based applications, expected Pr values are moderately high, while E_c values range from moderately low to high.[4, 5, 33, 34] In comparison to other ferroelectric materials, $Al_{1-x}Sc_xN$ stands out with notably high remnant polarization (70 to 140 $\mu C/cm^2$) and coercive field (2 to 8 MV/cm), showing values approximately 2 to 6 times and 2 to 3 times higher respectively than those of oxide perovskites and fluorite-structured ferroelectric materials.[4]

While achieving the desired remnant polarization for $Al_{1-x}Sc_xN$ is relatively feasible, the true challenge lies in precisely adjusting the coercive field value of $Al_{1-x}Sc_xN$ to meet the specific demands of various applications. A noteworthy limitation of $Al_{1-x}Sc_xN$ is its limited endurance, with the number of flipping bits close to 10^5.[35] The endurance of ferroelectric materials is typically proportional to the breakdown field (E_{bd}) to coercive field (E_c) ratio.[4] As $Al_{1-x}Sc_xN$ possesses a high coercive field value which results in a low E_{bd}/E_c ratio, consequently contributing to the observed low endurance.[35-37] Different crucial factors have been investigated over the years to control the coercive field, including the adjustment of alloying composition, strain engineering, film thickness, growth temperature, operating temperature, and applied frequency. Ryoichi Mizutani et al. demonstrated that the coercive field of $Al_{1-x}Sc_xN$ depends on thickness and measuring temperature[38], while Ved Gund et al. showed that E_c of $Al_{1-x}Sc_xN$ depends on applied frequency[39]. Tsai et al. demonstrated that ferroelectric properties depend on growth temperature.[36] Additionally, it has been observed that for $Al_{1-x}Sc_xN$, the coercive field decreases with increasing Sc concentration.[1] Leakage current, another important factor governing the performance of ferroelectric-based memory applications, is correlated with band gap and coercive field, determined by the percentage of Sc concentration in $Al_{1-x}Sc_xN$. Therefore, it is essential to consider the band gap effect while tailoring the coercive field.

Considering the aforementioned features, including Sc concentration (%), growth temperature (°C), film thickness (nm), frequency (kHz), temperature (K), and bandgap (eV), we developed a supervised machine learning model to predict the coercive field (MV/cm) as the target variable. This study aims to establish a reliable design space for $Al_{1-x}Sc_xN$ thin films fabricated using reactive sputtering by leveraging this model. These films are structured in Metal-Ferroelectric-Metal (MFM) or Metal-Insulator-Metal (MIM) configurations, with or without functional intermediate layers, and incorporate a single layer of $Al_{1-x}Sc_xN$. This specific fabrication process and structural configurations serve as a foundational architecture for non-volatile memory devices. By selecting specific growth conditions and testing parameters from the developed design space, researchers can effectively guide fabrication processes to achieve desired coercive field values. This applicability will streamline the fabrication approach and guide the experimental exploration effectively. This approach offers a comprehensive roadmap for selecting feature ranges and holds the potential to optimize future AlScN-related studies more effectively.

II. Methodology

Data collection and preprocessing:

Constructing an effective machine learning (ML) model demands high-quality data. While high-quality data and robust algorithms are the foundation of ML-based materials design, the selection of descriptors guided by domain knowledge significantly controls the model predictions. Essentially, the selection of appropriate descriptors relies on the target variables we aim to predict. This work utilized domain knowledge from previous experimental and computational studies to identify appropriate descriptors related to the target variable.

The methodology started with collecting data from the literature on sputter-deposited $Al_{1-x}Sc_xN$ for ferroelectric applications, reported since 2019 through the end of 2023, followed by a meticulous data refinement process to ensure dataset integrity and accuracy. A total of 84 data points were collected through literature surveys, focusing on the following descriptors: Sc concentration, growth temperature, film thickness, frequency, temperature, and bandgap, which were used to train the ML model. The refinement process involved eliminating redundancy in the dataset to mitigate noise and inconsistencies. The data was then split into training and test sets in an 80:20 ratio, following the Pareto principle, using a specific seed number (17) for consistency. To address challenges associated with small datasets and literature data ambiguity, imputation and standardization procedures were applied after data splitting. During imputation, the same seed number (17) was used to ensure reproducibility. Additionally, this process ensured that no data leakage occurred between the training and testing sets. A sophisticated imputation technique known as multivariate imputation was utilized to fill in missing values, specifically addressing the absence of seven growth temperature values. This method accounts for relationships and patterns among multiple variables rather than imputing values based on individual variables independently.

The Iterative Imputer class from scikit-learn was used for this purpose, along with a specific seed number. Standardization was then performed on the imputed training and test datasets using the StandardScaler library from scikit-learn, ensuring consistency across varied numerical ranges and units of descriptors. Finally, the training and testing datasets were saved separately after imputation and standardization for ML model building and evaluation.

Machine learning modeling:

Given the small dataset size, careful selection of the machine learning algorithm is essential for accurate target variable prediction.[40] Commonly employed ML algorithms for small datasets encompass MLR (Multiple Linear Regression), Lasso, Ridge, SVR (Support Vector Regression), PCR (Principle Component Regression), GPR (Gaussian Process Regression), and RF (Random Forest Regression).[40, 41] Regression methods, like those mentioned above, are fundamental tools in predicting and understanding relationships between variables. In the context of material science, regression models serve to elucidate the quantitative relationships between material properties and various factors, guiding the design and optimization of materials for specific applications. The training dataset was applied to these models for model selection. During the training process, all the models were tuned via hyperparameter tuning with k-fold (5-fold) cross-validation, except for MLR as it does not have any hyperparameters. In this work, K-fold cross-validation (K-fold CV) was chosen over leave-one-out cross-validation (LOOCV) despite the small dataset size. This decision was made because the dataset contains more than thirty data points, making K-fold CV a suitable choice.[40] While LOOCV is commonly preferred for very small datasets, its computational expense can become prohibitive as the dataset size increases.[40] During model tuning, several kernel functions with different parameters were tested for SVR and GPR. Evaluation metrics including RMSE and R-squared score were employed to assess the models on the unseen test dataset.

Additionally, cross-validated RMSE was calculated for each of the ML models to see the performance of the models on unseen data. Following the comparison of evaluation metrics, random forest came out as the best model. This ensemble learning method aggregates predictions from multiple decision trees to enhance stability while minimizing variance. The RandomForestRegressor from scikit-learn was employed, utilizing hyper-parameters such as n_estimators, max_depth, min_samples_split, min_samples_leaf, max_features, and criterion. These parameters were tuned using GridsearchCV with 5-fold cross-validation to prevent overfitting or underfitting. The performance of the trained and tuned RF model was evaluated on the test set. Additionally, the final model was assessed by employing different random seed numbers for data splitting, with consistent evaluation metrics across all splits, indicating stable predictions. The final model was deployed for further predictions.

Feature importance:

SHAP (SHapley Additive exPlanations) analysis was utilized to rank the features as per their importance and explain the output from the final ML model. To perform SHAP analysis, shap package from Python was used and then SHAP summary plot was constructed by using SHAP tree explainer. The SHAP tree explainer method is utilized to comprehend the inner construction of tree-based models like random forest in this case. This approach aggregates the computations linked with individual leaf nodes of the tree model, yielding a simplified explanation of the model's predictions with low-order complexity.[42]

Random dataset generation and new prediction:

Leveraging important features and domain knowledge, a random dataset was generated, focusing on three crucial features: Film thickness, Temperature, and Frequency. These features were selected based on their significance in material fabrication and testing processes. The dataset comprised 1,161,216 data points while keeping other feature values (Sc concentration, Growth temperature, and Bandgap) unchanged with those used in the initial dataset for model building and testing. Starting with film thickness, ranging from 9nm to 1000nm divided into 24 ranges, each containing 84 randomly generated data points. This range was carefully chosen ensuring a comprehensive spectrum of potential values observed in real-world scenarios. For example, film thickness variations documented in the literature[1, 38] helped divide the data into the ranges, aligning with experimental findings. Similarly, a total of 24 ranges were established for temperature, ranging from 273K to 700K, based on relevant literature sources.[38, 43] Frequencies utilized in hysteresis loop testing, typically falling between 1 and 100 kHz, leading to the creation of 24 ranges around these frequency values, thus capturing the essential nuances of experimental practices.[5, 38, 39]

By combining these ranges for film thickness, frequency, and temperature, we generated a comprehensive dataset of design space. This newly generated dataset incorporated other critical attributes, such as Sc concentration, Growth temperature, and Bandgap, while preserving their original values from the initial dataset. This integration process ensured the dataset's coherence and consistency, laying a solid foundation for subsequent analyses and machine learning modeling. The comprehensive flow chart for the above-mentioned procedures is depicted in Figure 1.

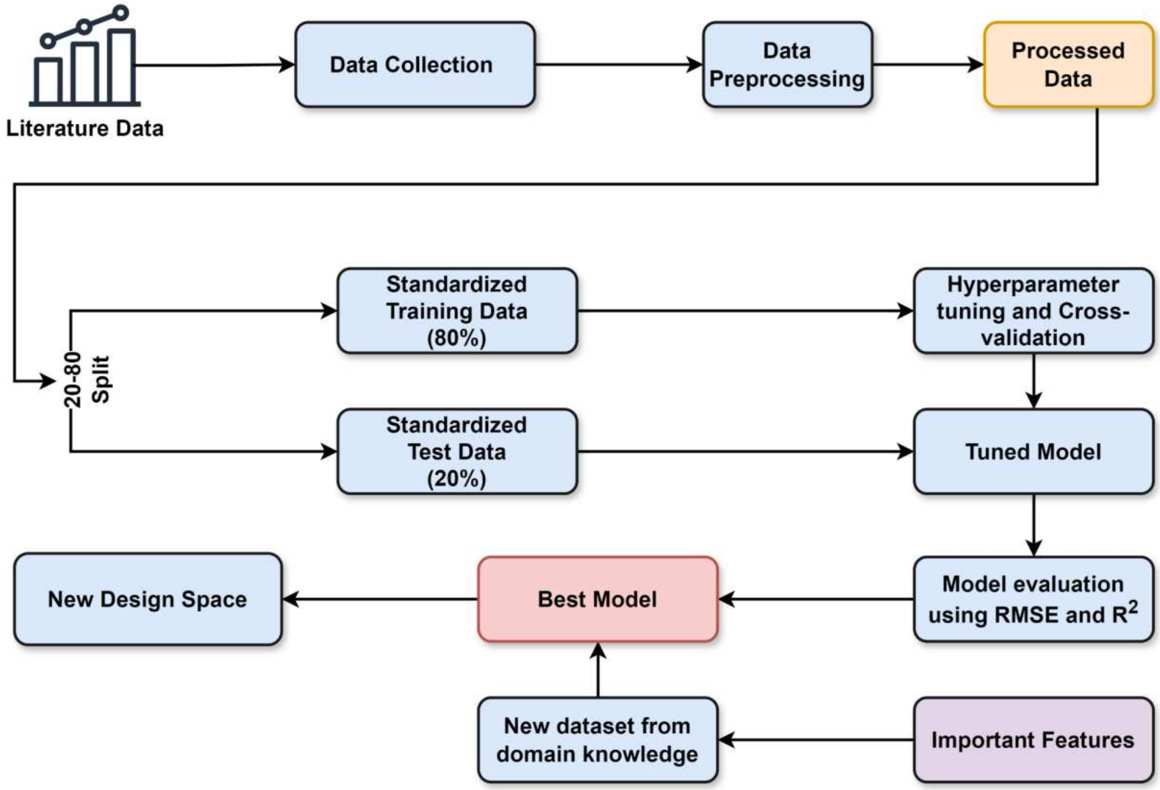

Figure 1: Comprehensive workflow of applied machine learning method

For more information on the dataset, including source references, hyperparameter search spaces, and the validation of the design space -please refer to the supplementary file. This additional information ensures clarity and supports the reproducibility of our study.

III. Results and discussion

The process of selecting an appropriate regression model out of the considered seven models involved a careful comparison of R-squared (R^2) and Root Mean Square Error (RMSE) values as a measure of model performance. While R^2 evaluates how well the model explains the variability in the data, RMSE provides insight into the accuracy of individual predictions, ensuring a balanced assessment of model fit and predictive accuracy. Among these models, the Random Forest (RF) model emerged as the most promising candidate, exhibiting an impressive R^2 value of 88% for test dataset. This high R^2 value signifies that the RF model shows good accuracy in predicting the target variable when applied to unseen test data (Figure 2a). Moreover, the RMSE (Figure 2b) value, which quantifies the average deviation of predicted values from the actual values, was substantially lower for the RF model compared to other regression models, standing at 0.52 for the test data. This lower RMSE and higher R^2 values suggest the RF model's superior predictive accuracy and efficacy in capturing the underlying patterns within the dataset.

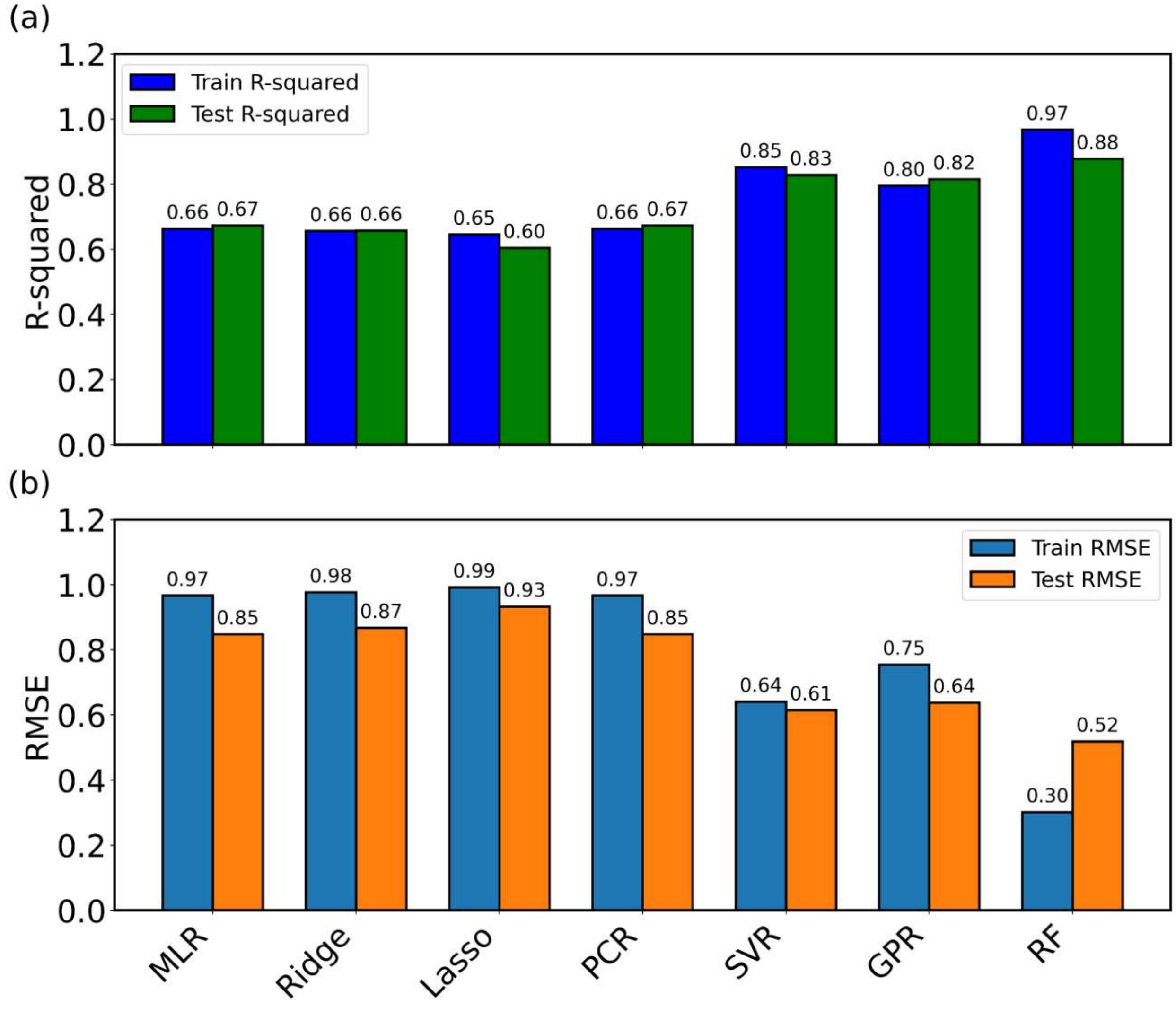

Figure 2**:** Evaluation of regression models using R^2 and RMSE metrics

Additionally, to ensure the robustness of the model, hyperparameter tuning and cross-validation were performed, and the RF model consistently exhibited the lowest Cross-Validated RMSE (CV RMSE) among all the models. This rigorous evaluation process aimed to mitigate the risks of overfitting or underfitting, thus enhancing the reliability and generalization capability of the selected RF model. Finally, the parity plot generated for the RF model further corroborated its predictive prowess, as evidenced by the minimal deviation observed around the diagonal line, indicating a close alignment between predicted and actual values (Figure 3).

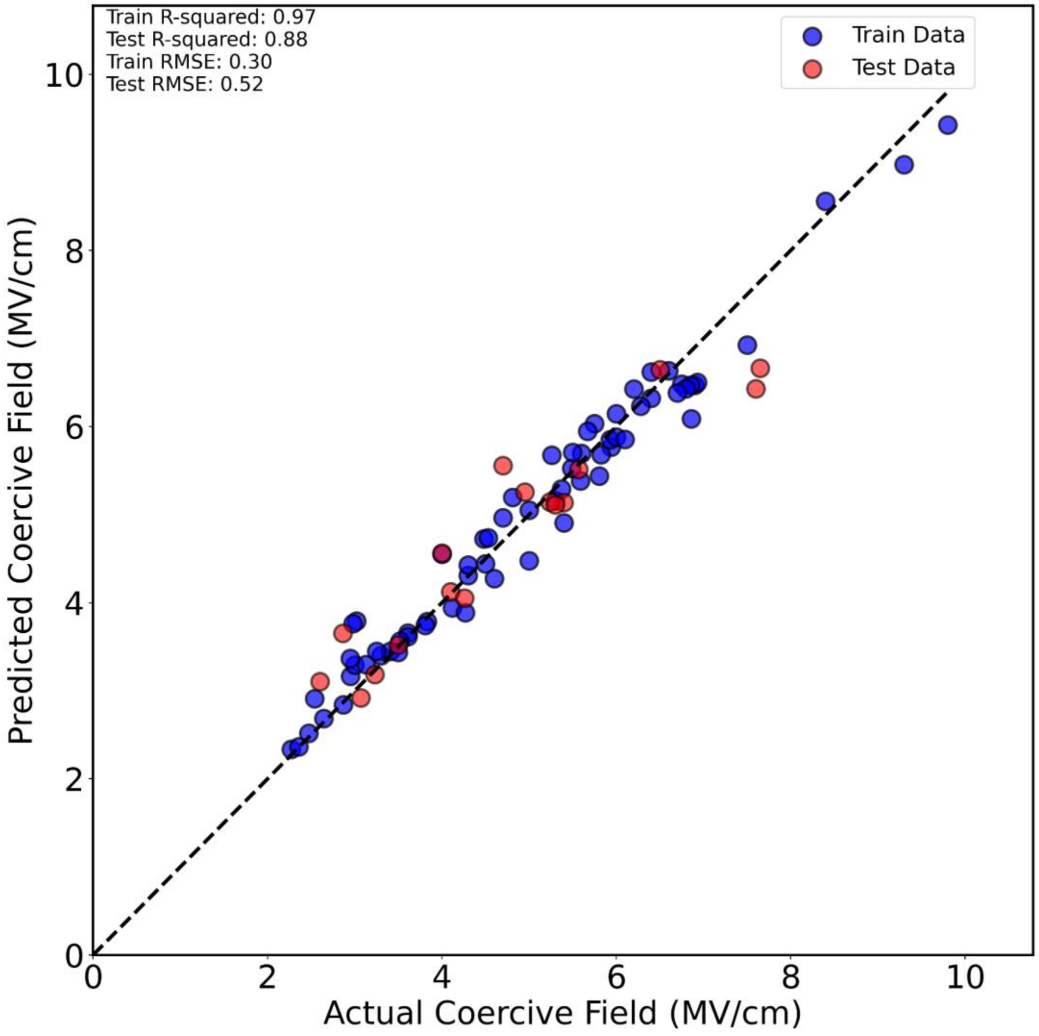

Figure 3: Parity plot of the best model (Random Forest)

According to the SHAP summary plot, film thickness emerged as the most significant feature, while band gap was identified as the least significant feature (Figure 4). This plot also suggests that film thickness, temperature, and scandium concentration negatively impact the coercive field, while frequency and growth temperature have a slight positive influence. Following the evaluation of feature importance, the first five significant feature combinations related to predicted coercive field values have been extracted to construct the design space.

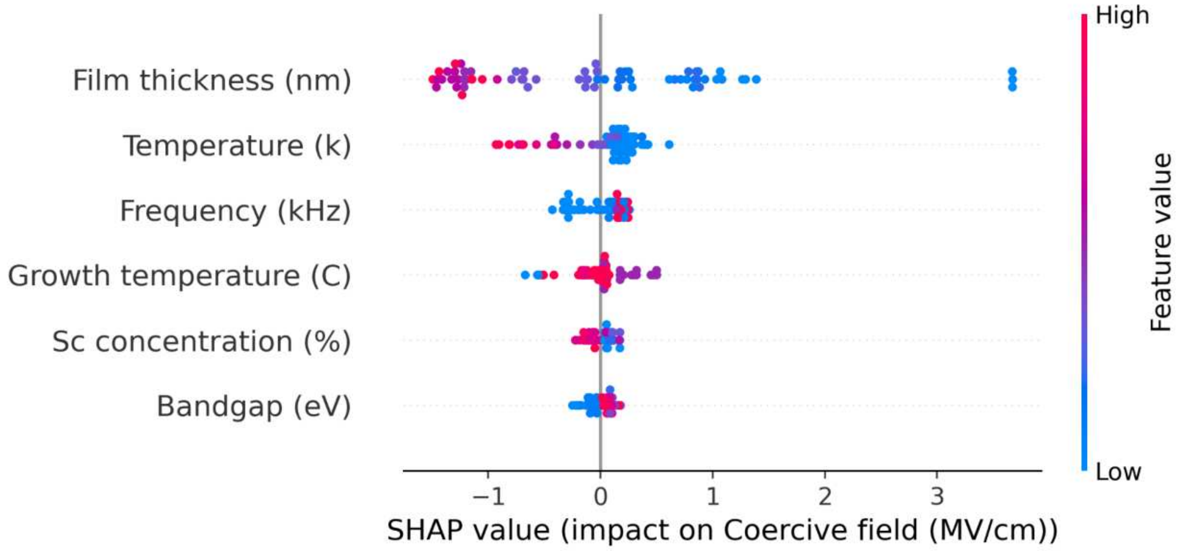

Figure 4: Feature importance ranking from SHAP summary plot

Bandgap was excluded from constructing the design space as it does not directly impact the coercive field value and demonstrated less importance in the feature analysis. Also, previous studies showed that Bandgap depends on Sc concentration.[44,45] Despite the limited variability of Sc concentration as indicated by the SHAP analysis, it was still considered in predicting coercive field values. This decision was guided by the significant impact of Sc concentration on the coercive field, which was further supported by the empirical equation,

$$E_C(x) = -15x + 8.35 \text{ (MV/cm)} \qquad (1)$$

where $0 < x < 0.43$, correlating the coercive field with the scandium percentage.[36, 46]

The influence of the scandium percentage on coercive field value for $Al_{1-x}Sc_xN$ has been studied over the years revealing a decrease in coercive field value with increasing scandium percentage. However, increasing scandium percentages have been associated with a degradation in crystal quality, directly impacting the c/a ratio effect on the switching ability of the polarization states.[39, 47, 48] The crystal structure and c/a ratio are crucial parameters for controlling the coercive field, and they are directly influenced by the scandium percentages. Hence, finding the ideal scandium percentage poses a challenge as it must achieve a balance between achieving optimal crystal quality and attaining the targeted coercive field value simultaneously. In the newly generated dataset, we incorporated all previously utilized scandium percentage values to predict the coercive field using our ML model. Notably, we didn't introduce any new scandium percentage values to this dataset because the existing ones already covered the important concentration values, contributing solely to the effective coercive field ranges.[1, 49] Moreover, the growth temperature directly affects crystal quality and levels of defects, thus it is anticipated to influence the ferroelectric properties.[36] Similarly, the approach for growth temperature followed that of the Sc concentration, with the temperature values from the original dataset being reused in the generation of the random dataset.

The developed Random Forest (RF) model effectively predicted coercive field values for a vast dataset comprising 1,161,216 randomly generated data points. These predictions are visually depicted in Figure 5 and quantitatively represented in Table 1. Notably, the predicted coercive field values in Table 1 depict a predominant range, typically ranging between 3 and 4.5, indicating the most probable outcomes predicted by the RF model.

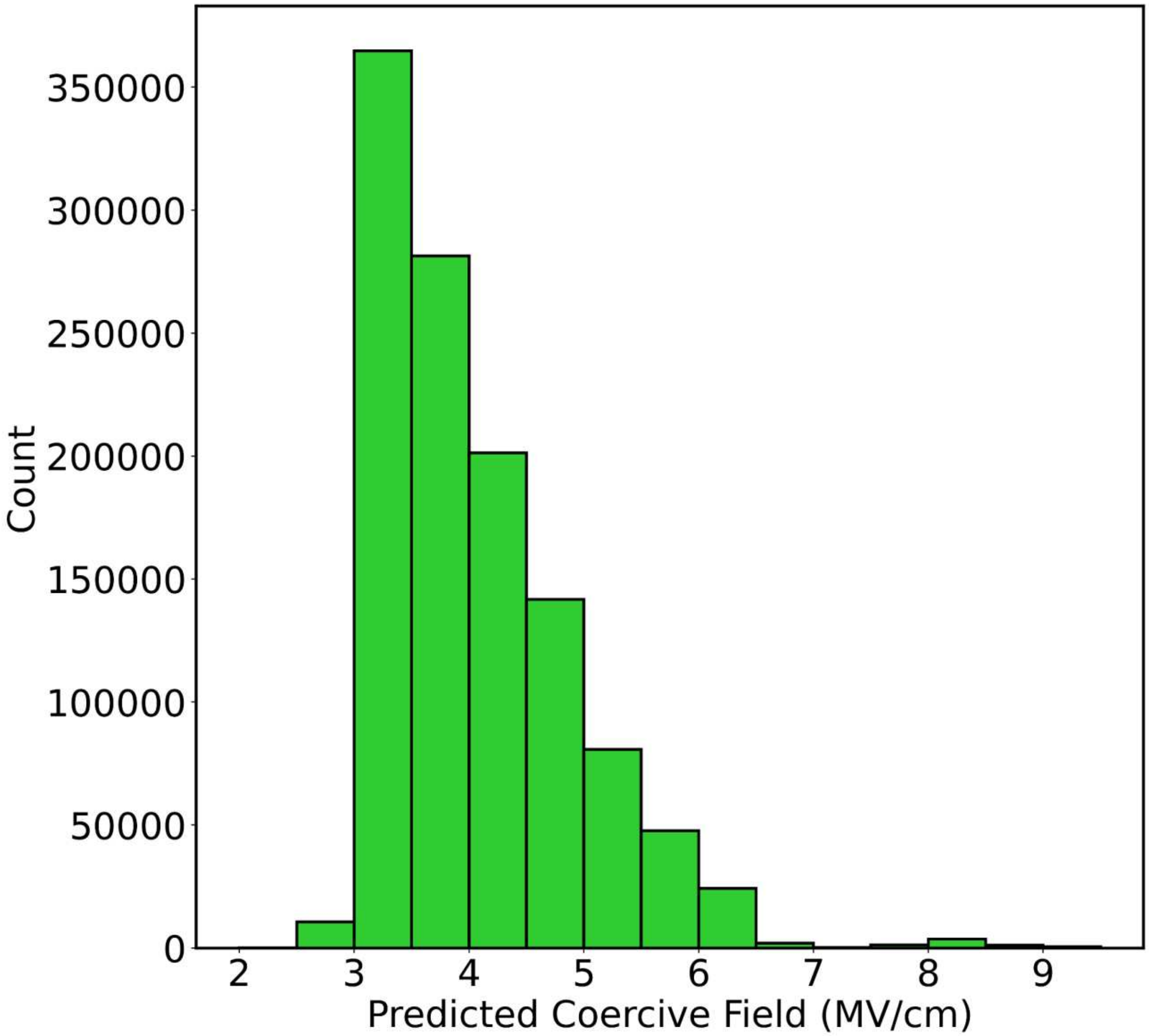

Figure 5: Predicted coercive field for the new dataset using the best ML model

Table 1: Predicted coercive field range and their corresponding relative frequency for important features of new dataset.

Range	Count	Relative Frequency (%)
2.0-2.5	90	0.0078
2.5-3.0	10653	0.9174
3.0-3.5	364784	31.4140
3.5-4.0	281381	24.2316
4.0-4.5	201289	17.3343
4.5-5.0	141680	12.2010
5.0-5.5	80717	6.9511
5.5-6.0	47643	4.1029
6.0-6.5	24261	2.0893
6.5-7.0	1987	0.1711
7.0-7.5	228	0.01964
7.5-8.0	1218	0.1049
8.0-8.5	3649	0.3142
8.5-9.0	1143	0.0984
9.0-9.5	493	0.0425

Following the prediction of coercive field values and their integration into the newly generated dataset, an Exploratory Data Analysis (EDA) approach is adopted to gain insights into the relationship between the predicted coercive field and important features. Utilizing Matplotlib's hexbin plots, the distribution and density of predicted coercive field values are visualized against different material parameters in Figure 6. Each subplot represents a specific feature, such as film thickness, frequency, temperature, Sc concentration, and growth temperature, plotted against the predicted coercive field. The hexbin plots enable the visualization of data density, where color intensity represents the count of data points within each bin. This helps to see patterns and connections between the predicted coercive field and the features. This understanding can then be used to improve material design and optimization strategies. These hexbin plots offer a comprehensive overview of the relationship between predicted coercive field and material features, facilitating a deeper understanding of the design space. By analyzing these plots, it is possible to identify influential material parameters and their impact on coercive field prediction, informing the development of targeted material fabrication and testing strategies.

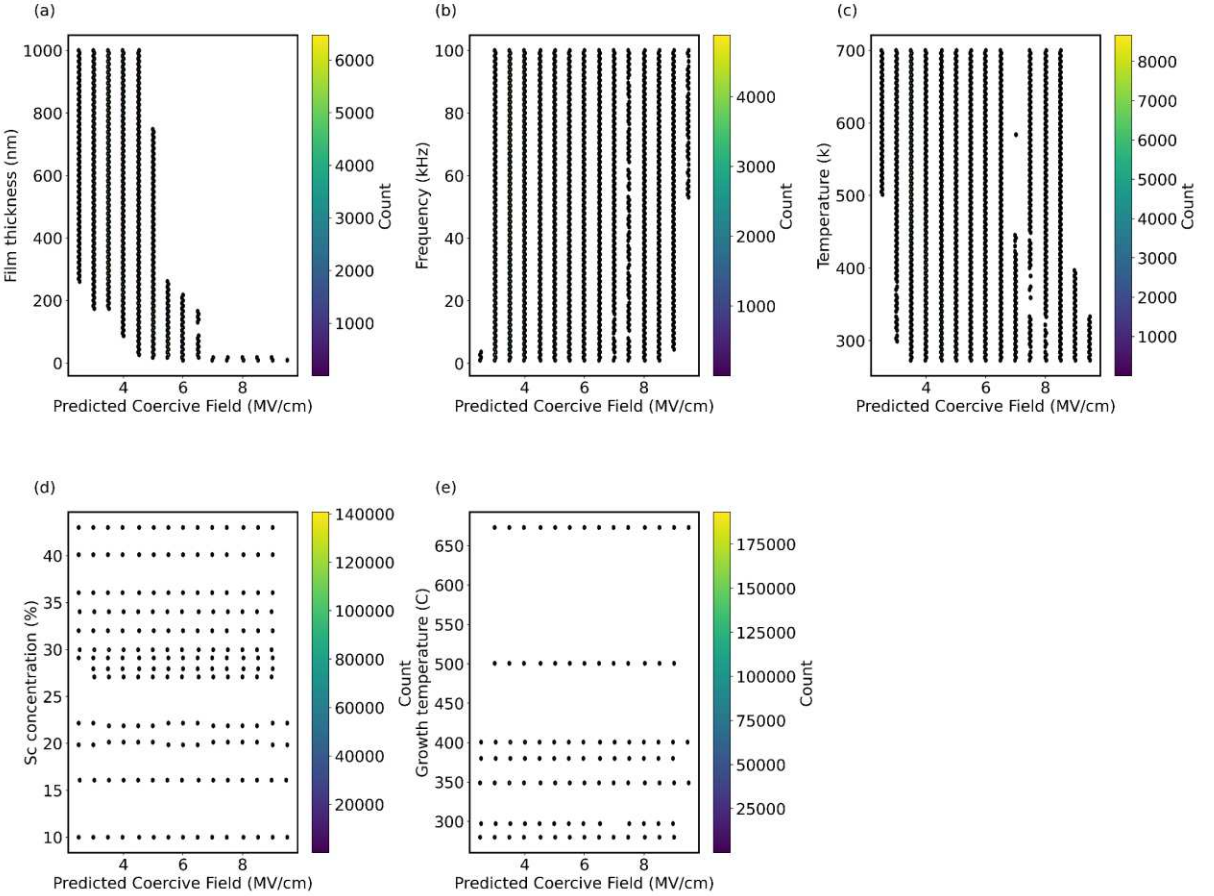

Figure 6: Important feature range extracted for all the predicted coercive field values (a) variation in film thickness with coercive field (b) variation in frequency with coercive field (c) variation in temperature with coercive field (d) variation in Sc concentration with coercive field (e) variation in growth temperature with coercive field

In addition to the exploratory data analysis, a further step is taken to delve into the relationship between the predicted coercive field and material features. While hexbin plots offer valuable insights, not all material features will show clear visual trends, therefore, to gain a more precise understanding, Spearman's rank-order correlation coefficient is calculated in Table 2. This quantitative analysis offers a systematic approach to assessing the strength and direction of the relationship between the predicted coercive field and other variables. By excluding less influential features such as 'Bandgap (eV)', the focus is refined towards identifying significant correlations with other parameters. This analytical step aims to provide a clearer and more concise overview of the trends and correlations within the dataset, complementing the insights obtained from visualizations.

Table 2: Spearman correlation coefficients for predicted coercive field

Features	**Spearman Correlation Coefficient**
Film thickness (nm)	-0.5554
Frequency (kHz)	0.1134
Temperature (k)	-0.5946
Sc concentration (%)	-0.1011
Growth temperature (°C)	0.0415

The Spearman's correlation coefficients for the 'Coercive Field' reveal the strength of the connection between each material feature and the predicted coercive field value, offering valuable insights into feature importance. This quantitative assessment enables anyone to discern subtle relationships that may not be immediately apparent from visualizations alone. By integrating both exploratory visualizations and quantitative correlation analysis, anyone can gain a comprehensive understanding of the design space. Which will identify influential material parameters and guide the development of targeted material fabrication and testing strategies. This holistic approach enhances the efficiency and effectiveness of the material design process, facilitating the optimization of $Al_{1-x}Sc_xN$ with desired coercive field range.

The importance of film thickness in predicting coercive field can be explained by the dependence of coercive field (E_c) on the polarization switching voltage. Both experimental and theoretical investigations have established that E_c decreases as thickness increases.[38, 50, 51] The semiempirical relationship describing size-effect phenomena in ferroelectric materials is articulated by the Janovec−Kay−Dunn (JKD) law, represented as $E_c \propto d^{-2/3}$, where E_c denotes the coercive field and d signifies the average crystallite size.[38, 50, 51] It's noted that for $Al_{1-x}Sc_xN$, this law remains applicable for thicknesses exceeding 10nm.[4] In this study, the developed ML model accurately forecasted coercive field values for random thickness values ranging from 9nm to 1000nm. From Figure 6a, it's evident that as the thickness increases, the coercive field value decreases. Furthermore, the negative Spearman correlation coefficient for film thickness from Table 2 supports this observation. Previous studies clearly explained the root cause of this size-dependent phenomenon as the presence of a space charge-induced depletion layer or non-ferroelectric blocking layer which eventually leads to the depolarizing field at the interfaces.[52, 53]

In addition to thickness, previous findings indicate a direct impact of temperature on the coercive field of ferroelectric materials.[38, 54, 55] The temperature and coercive field in ferroelectric materials are related linearly and decrease with increasing temperature.[38, 54, 56] We utilized our developed ML model to predict coercive fields for random temperature values within the range of 300K to 700K. Figure 6c illustrates a negative correlation between coercive field and operating temperature, that is further supported by the negative Spearman correlation coefficient from Table 2. Additionally, the coercive field value tends to increase with frequency due to the inertia of polarization reversal.[57] Over time, researchers have investigated the impact of frequency on the coercive field in ferroelectric materials, developing various model-based theories that directly relate to domain wall motion and growth.[58-61] Previous experimental studies on $Al_{1-x}Sc_xN$ have typically employed testing frequencies ranging from 1kHz to 100kHz. Consistent with this range, random frequency values were created within this spectrum and our established ML model was used to predict coercive field for each frequency. A positive correlation between frequency and predictive coercive field is evident from the Spearman correlation coefficient in Table 2. Increasing the operating frequency beyond 100kHz can reduce the contribution of leakage current, as the frequency of the applied voltage increases, misalignment between the voltage and current response arises owing to the RC delay which poses a significant challenge in accurately measuring the P-E curve.[62] Also, there is a positive correlation between growth temperature and coercive field according to Table 2.

To illustrate the application of our findings, we can explore the predicted coercive field and connected features depicted in Figure 6 using a specific example. Where Figure 7 illustrates a particular design space with a coercive field range of 2.5 MV/cm to 3 MV/cm alongside the corresponding ranges for relevant material properties that influence this target property. This visual guide enables researchers to discern preferred values for thickness, temperature, frequency, scandium percentage, and growth temperature within the desired coercive field range.

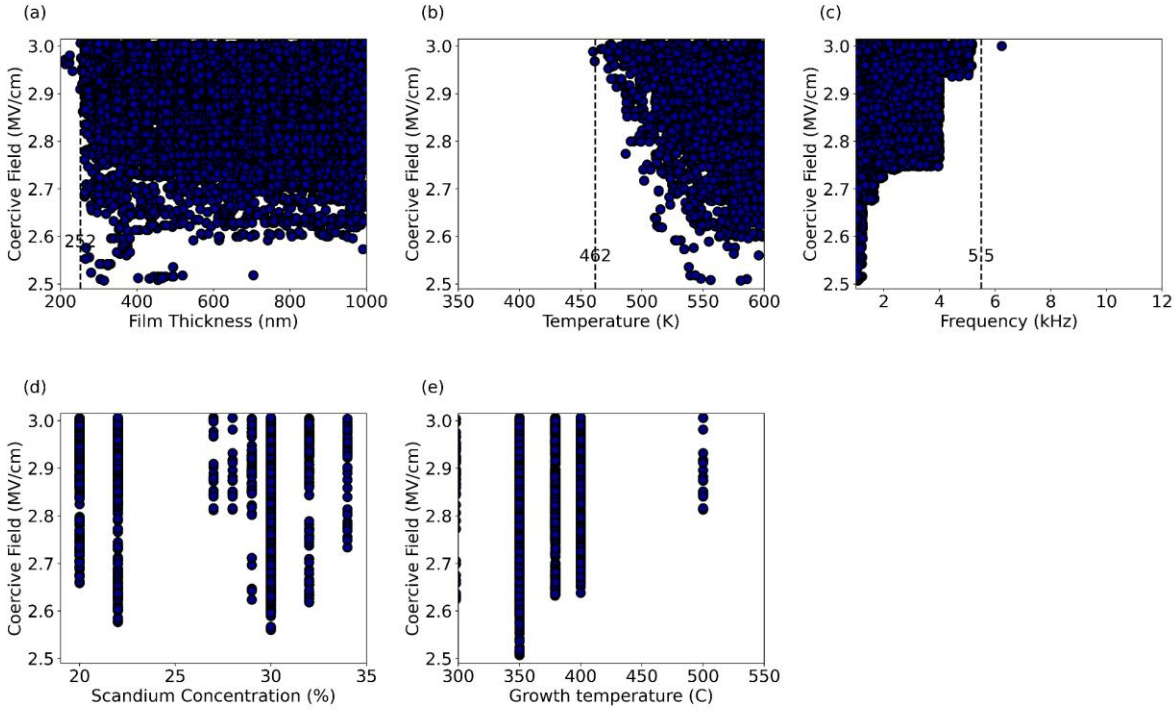

Figure 7: Design space for fabricating sputter-deposited thin film within coercive field range 2.5 to 3.0 for specific scandium concentration (%) in the range of 20 to 35

Building upon this illustration, exploring the design space begins with a systematic search depending on the predicted coercive field values. This systematic search is carefully guided by the specification of input ranges tailored to the unique characteristics of the dataset, facilitating iterative exploration through incremental coercive field ranges. As each subset corresponding to the specified coercive field range is dynamically identified, the analysis offers a detailed examination. For each coercive field range, scatter plots are generated, illustrating the coercive field against individual material features including film thickness, temperature, frequency, scandium concentration, and growth temperature. The incorporation of perpendicular lines serves to highlight key values within the dataset, thereby enriching the analysis process. Through these visualizations, distinct trends and patterns emerge, fostering a comprehensive understanding of the relationship between coercive field and material parameters across various ranges. This systematic approach not only facilitates effective navigation and dissection of the design space but also provides a guiding framework for the refinement of material fabrication and testing strategies. This comprehensive visual analysis not only enhances the comprehension of material-property relationships but also furnishes practical insights for the development of tailored $Al_{1-x}Sc_xN$ with desired coercive field characteristics.

IV. Conclusion

In this study, we successfully employed machine learning techniques to predict and optimize the coercive field of $Al_{1-x}Sc_xN$ thin films fabricated using reactive sputtering. These films consist of a single $Al_{1-x}Sc_xN$ layer incorporated with different layer stacking combinations to suit non-volatile memory applications. The Random Forest model developed in this work, validated through comprehensive cross-validation, exhibited a high predictive accuracy, evidenced by an R^2 value of 0.88, confirming the robustness of the approach. Leveraging this ML model, the development of an extensive design space enables the precise selection of key parameters, including film thickness, scandium concentration, and growth temperature. This approach significantly reduces the time and resources typically required for experimental investigations. The model's predictions delineate a predominant coercive field range of 3 MV/cm to 4.5 MV/cm, with a potential minimum range of 2.5 MV/cm to 3 MV/cm, providing a valuable framework for guiding future experimental work and device fabrication. While the findings of this study establish a solid foundation for optimizing $Al_{1-x}Sc_xN$ thin films, they also highlight new directions for further research. Future investigations could extend this methodology to other ferroelectric materials and assess the model's generalizability across varying operational conditions. Such advancements will contribute to the broader development of ferroelectric materials, with significant implications for the design and performance of next-generation non-volatile memory devices.

ACKNOWLEDGMENTS

The authors acknowledge the support from National Science Foundation (NSF) under DMR (grant# 2114595 and 2145091).

REFERENCES

1. Fichtner S, Wolff N, Lofink F, Kienle L, Wagner B. AlScN: A III-V semiconductor based ferroelectric. Journal of Applied Physics. 2019;125(11).
2. Wilson RM. Switching the polarization in metal-nitride ferroelectrics. Physics Today. 2023;2023(06).
3. Moriwake H, Yokoi R, Taguchi A, Ogawa T, Fisher CAJ, Kuwabara A, et al. A computational search for wurtzite-structured ferroelectrics with low coercive voltages. APL Materials. 2020;8(12).
4. Kim K-H, Karpov I, Olsson RH, Jariwala D. Wurtzite and fluorite ferroelectric materials for electronic memory. Nature Nanotechnology. 2023;18(5):422-41.
5. Kim KD, Lee YB, Lee SH, Lee IS, Ryoo SK, Byun S, et al. Evolution of the Ferroelectric Properties of AlScN Film by Electrical Cycling with an Inhomogeneous Field Distribution. Advanced Electronic Materials. 2023;9(5).
6. Cheng C-H, Chin A. Low-Leakage-Current DRAM-Like Memory Using a One-Transistor Ferroelectric MOSFET With a Hf-Based Gate Dielectric. IEEE Electron Device Letters. 2014;35(1):138-40.
7. Kim JY, Choi M-J, Jang HW. Ferroelectric field effect transistors: Progress and perspective. APL Materials. 2021;9(2).
8. Valasek J. Piezo-Electric and Allied Phenomena in Rochelle Salt. Physical Review. 1921;17(4):475-81.
9. Fousek J. Joseph Valasek and the discovery of ferroelectricity. Proceedings of 1994 IEEE International Symposium on Applications of Ferroelectrics1994. p. 1-5.
10. Muralt P, Polcawich RG, Trolier-McKinstry S. Piezoelectric Thin Films for Sensors, Actuators, and Energy Harvesting. MRS Bulletin. 2011;34(9):658-64.
11. Zhang S, Xia R, Lebrun L, Anderson D, Shrout TR. Piezoelectric materials for high power, high temperature applications. Materials Letters. 2005;59(27):3471-5.
12. Guido R, Lomenzo PD, Islam MR, Wolff N, Gremmel M, Schönweger G, et al. Thermal Stability of the Ferroelectric Properties in 100 nm-Thick Al0.72Sc0.28N. ACS Applied Materials & Interfaces. 2023;15(5):7030-43.
13. Wang P, Wang D, Mondal S, Hu M, Liu J, Mi Z. Dawn of nitride ferroelectric semiconductors: from materials to devices. Semiconductor Science and Technology. 2023;38(4).

14. Banerjee W, Kashir A, Kamba S. Hafnium Oxide (HfO2) – A Multifunctional Oxide: A Review on the Prospect and Challenges of Hafnium Oxide in Resistive Switching and Ferroelectric Memories. Small. 2022;18(23).
15. Martin LW, Rappe AM. Thin-film ferroelectric materials and their applications. Nature Reviews Materials. 2016;2(2).
16. Hayden J, Hossain MD, Xiong Y, Ferri K, Zhu W, Imperatore MV, et al. Ferroelectricity in boron-substituted aluminum nitride thin films. Physical Review Materials. 2021;5(4).
17. Wang D, Wang P, Wang B, Mi Z. Fully epitaxial ferroelectric ScGaN grown on GaN by molecular beam epitaxy. Applied Physics Letters. 2021;119(11).
18. Calderon S, Hayden J, Baksa SM, Tzou W, Trolier-McKinstry S, Dabo I, et al. Atomic-scale polarization switching in wurtzite ferroelectrics. Science. 2023;380(6649):1034-8.
19. Farrer N, Bellaiche L. Properties of hexagonal ScN versus wurtzite GaN and InN. Physical Review B. 2002;66(20).
20. Ranjan V, Bellaiche L, Walter EJ. Strained Hexagonal ScN: A Material with Unusual Structural and Optical Properties. Physical Review Letters. 2003;90(25).
21. Tasnádi F, Alling B, Höglund C, Wingqvist G, Birch J, Hultman L, et al. Origin of the Anomalous Piezoelectric Response in WurtziteScxAl1−xNAlloys. Physical Review Letters. 2010;104(13).
22. Zhang S, Holec D, Fu WY, Humphreys CJ, Moram MA. Tunable optoelectronic and ferroelectric properties in Sc-based III-nitrides. Journal of Applied Physics. 2013;114(13).
23. Akiyama M, Kano K, Teshigahara A. Influence of growth temperature and scandium concentration on piezoelectric response of scandium aluminum nitride alloy thin films. Applied Physics Letters. 2009;95(16).
24. Zywitzki O, Modes T, Barth S, Bartzsch H, Frach P. Effect of scandium content on structure and piezoelectric properties of AlScN films deposited by reactive pulse magnetron sputtering. Surface and Coatings Technology. 2017;309:417-22.
25. Zukauskaite A, Wingqvist G, Palisaitis J, Jensen J, Persson POÅ, Matloub R, et al. Microstructure and dielectric properties of piezoelectric magnetron sputtered w-ScxAl1−xN thin films. Journal of Applied Physics. 2012;111(9).
26. Matloub R, Hadad M, Mazzalai A, Chidambaram N, Moulard G, Sandu CS, et al. Piezoelectric Al1−xScxN thin films: A semiconductor compatible solution for mechanical energy harvesting and sensors. Applied Physics Letters. 2013;102(15).
27. Mertin S, Heinz B, Rattunde O, Christmann G, Dubois M-A, Nicolay S, et al. Piezoelectric and structural properties of c-axis textured aluminium scandium nitride thin films up to high scandium content. Surface and Coatings Technology. 2018;343:2-6.
28. Fichtner S, Reimer T, Chemnitz S, Lofink F, Wagner B. Stress controlled pulsed direct current co-sputtered Al1−xScxN as piezoelectric phase for micromechanical sensor applications. APL Materials. 2015;3(11).
29. Su J, Niekiel F, Fichtner S, Thormaehlen L, Kirchhof C, Meyners D, et al. AlScN-based MEMS magnetoelectric sensor. Applied Physics Letters. 2020;117(13).
30. Yarar E, Fichtner S, Hayes P, Piorra A, Reimer T, Lisec T, et al. MEMS-Based AlScN Resonating Energy Harvester With Solidified Powder Magnet. Journal of Microelectromechanical Systems. 2019;28(6):1019-31.
31. Gu-Stoppel S, Lisec T, Fichtner S, Funck N, Claus M, Wagner B, et al. AlScN based MEMS quasi-static mirror matrix with large tilting angle and high linearity. Sensors and Actuators A: Physical. 2020;312.
32. Toprasertpong K, Takenaka M, Takagi S. Memory Window in Ferroelectric Field-Effect Transistors: Analytical Approach. IEEE Transactions on Electron Devices. 2022;69(12):7113-9.

33. Schenk T, Pešić M, Slesazeck S, Schroeder U, Mikolajick T. Memory technology—a primer for material scientists. Reports on Progress in Physics. 2020;83(8).
34. Deng S, Zhao Z, Kurinec S, Ni K, Xiao Y, Yu T, et al. Overview of Ferroelectric Memory Devices and Reliability Aware Design Optimization. Proceedings of the 2021 Great Lakes Symposium on VLSI2021. p. 473-8.
35. Mikolajick T, Slesazeck S, Mulaosmanovic H, Park MH, Fichtner S, Lomenzo PD, et al. Next generation ferroelectric materials for semiconductor process integration and their applications. Journal of Applied Physics. 2021;129(10).
36. Tsai S-L, Hoshii T, Wakabayashi H, Tsutsui K, Chung T-K, Chang EY, et al. Room-temperature deposition of a poling-free ferroelectric AlScN film by reactive sputtering. Applied Physics Letters. 2021;118(8).
37. Zheng JX, Wang D, Musavigharavi P, Fiagbenu MMA, Jariwala D, Stach EA, et al. Electrical breakdown strength enhancement in aluminum scandium nitride through a compositionally modulated periodic multilayer structure. Journal of Applied Physics. 2021;130(14).
38. Mizutani R, Yasuoka S, Shiraishi T, Shimizu T, Uehara M, Yamada H, et al. Thickness scaling of (Al0.8Sc0.2)N films with remanent polarization beyond 100 μC cm−2 around 10 nm in thickness. Applied Physics Express. 2021;14(10).
39. Gund V, Davaji B, Lee H, Casamento J, Xing HG, Jena D, et al. Towards Realizing the Low-Coercive Field Operation of Sputtered Ferroelectric ScxAl1-xN. 2021 21st International Conference on Solid-State Sensors, Actuators and Microsystems (Transducers)2021. p. 1064-7.
40. Xu P, Ji X, Li M, Lu W. Small data machine learning in materials science. npj Computational Materials. 2023;9(1).
41. Stoll A, Benner P. Machine learning for material characterization with an application for predicting mechanical properties. GAMM-Mitteilungen. 2021;44(1).
42. Anjum M, Khan K, Ahmad W, Ahmad A, Amin MN, Nafees A. New SHapley Additive ExPlanations (SHAP) Approach to Evaluate the Raw Materials Interactions of Steel-Fiber-Reinforced Concrete. Materials. 2022;15(18).
43. Drury D, Yazawa K, Zakutayev A, Hanrahan B, Brennecka G. High-Temperature Ferroelectric Behavior of Al0.7Sc0.3N. Micromachines. 2022;13(6).
44. Deng R, Evans SR, Gall D. Bandgap in Al1−xScxN. Applied Physics Letters. 2013;102(11).
45. Baeumler M, Lu Y, Kurz N, Kirste L, Prescher M, Christoph T, et al. Optical constants and band gap of wurtzite Al1−xScxN/Al2O3 prepared by magnetron sputter epitaxy for scandium concentrations up to x = 0.41. Journal of Applied Physics. 2019;126(4).
46. Fichtner S, Lofink F, Wagner B, Schonweger G, Kreutzer T-N, Petraru A, et al. Ferroelectricity in AlScN: Switching, Imprint and sub-150 nm Films. 2020 Joint Conference of the IEEE International Frequency Control Symposium and International Symposium on Applications of Ferroelectrics (IFCS-ISAF)2020. p. 1-4.
47. Urban DF, Ambacher O, Elsässer C. First-principles calculation of electroacoustic properties of wurtzite (Al,Sc)N. Physical Review B. 2021;103(11).
48. Yazawa K, Drury D, Zakutayev A, Brennecka GL. Reduced coercive field in epitaxial thin film of ferroelectric wurtzite Al0.7Sc0.3N. Applied Physics Letters. 2021;118(16).
49. Yasuoka S, Shimizu T, Tateyama A, Uehara M, Yamada H, Akiyama M, et al. Effects of deposition conditions on the ferroelectric properties of (Al1−xScx)N thin films. Journal of Applied Physics. 2020;128(11).
50. Xu R, Gao R, Reyes-Lillo SE, Saremi S, Dong Y, Lu H, et al. Reducing Coercive-Field Scaling in Ferroelectric Thin Films via Orientation Control. ACS Nano. 2018;12(5):4736-43.
51. Li KT, Lo VC. Simulation of thickness dependence in ferroelectric thin films. Solid State Communications. 2004;132(1):49-54.

52. Tagantsev AK, Stolichnov IA. Injection-controlled size effect on switching of ferroelectric thin films. Applied Physics Letters. 1999;74(9):1326-8.
53. Larsen PK, Dormans GJM, Taylor DJ, van Veldhoven PJ. Ferroelectric properties and fatigue of PbZr0.51Ti0.49O3 thin films of varying thickness: Blocking layer model. Journal of Applied Physics. 1994;76(4):2405-13.
54. Gund V, Davaji B, Lee H, Asadi MJ, Casamento J, Xing HG, et al. Temperature-dependent Lowering of Coercive Field in 300 nm Sputtered Ferroelectric Al0.70Sc0.30N. 2021 IEEE International Symposium on Applications of Ferroelectrics (ISAF)2021. p. 1-3.
55. Zhu W, Hayden J, He F, Yang J-I, Tipsawat P, Hossain MD, et al. Strongly temperature dependent ferroelectric switching in AlN, Al1-xScxN, and Al1-xBxN thin films. Applied Physics Letters. 2021;119(6).
56. Bo H, Meng Q, Hu H, Zhao H, Zhang Z, Zhang Q, et al. Temperature-dependent ferroelectric properties of near stoichiometric lithium niobate single crystal. Applied Physics A. 2018;124(10).
57. Chen Z, Zhang Y, Li S, Lu X-M, Cao W. Frequency dependence of the coercive field of 0.71Pb(Mg1/3Nb2/3)O3-0.29PbTiO3 single crystal from 0.01 Hz to 5 MHz. Applied Physics Letters. 2017;110(20).
58. Hu J, Hossain ME, Li J. Investigation on frequency-dependent hysteresis loops of ferroelectric materials. Smart Materials and Structures. 2019;28(12).
59. Hwang SC, Lynch CS, McMeeking RM. Ferroelectric/ferroelastic interactions and a polarization switching model. Acta Metallurgica et Materialia. 1995;43(5):2073-84.
60. Chen W, Lynch CS. A micro-electro-mechanical model for polarization switching of ferroelectric materials. Acta Materialia. 1998;46(15):5303-11.
61. Chen X, Fang DN, Hwang KC. Micromechanics simulation of ferroelectric polarization switching. Acta Materialia. 1997;45(8):3181-9.
62. Damjanovic D. Logarithmic frequency dependence of the piezoelectric effect due to pinning of ferroelectric-ferroelastic domain walls. Physical Review B. 1997;55(2):R649-R52.